

# SABER: A Systems Approach to Blur Estimation and Reduction in X-ray Imaging

K. Aditya Mohan, *Member, IEEE*, Robert M. Panas, and Jefferson A. Cuadra,

**Abstract**—Blur in X-ray radiographs not only reduces the sharpness of image edges but also reduces the overall contrast. The effective blur in a radiograph is the combined effect of blur from multiple sources such as the detector panel, X-ray source spot, and system motion. In this paper, we use a systems approach to model the point spread function (PSF) of the effective radiographic blur as the convolution of multiple PSFs, where each PSF models one of the various sources of blur. Then, we present a numerical optimization algorithm for estimating each PSF from multiple radiographs acquired at different X-ray source to object (SOD) and object to detector distances (ODD). Finally, we computationally reduce blur in radiographs using deblurring algorithms that use the estimated PSFs from the previous step. Our approach to estimate and reduce blur is called SABER, which is an acronym for systems approach to blur estimation and reduction.

**Index Terms**—Blur, deblur, optimization, algorithm, radiography, tomography, source blur, detector blur, motion blur, deconvolution, model estimation, high resolution.

## I. INTRODUCTION

X-ray imaging systems are widely used for 2D and 3D non-destructive characterization and visualization of a wide range of objects. The ability of X-rays to penetrate deep inside a material makes it a useful tool to visualize the interior morphology of objects. X-ray imaging is very popular in applications such as industrial imaging [1]–[4], medical diagnosis [5], [6], and border security [4], [7]–[9]. A schematic representation of a typical cone-beam X-ray imaging system is shown in Fig. 1. Here, an object is exposed to a diverging beam of X-ray radiation that is generated by a X-ray source. The X-rays get attenuated as they propagate through the object and an image of the attenuated X-ray intensity is recorded by a detector consisting of a flat-panel 2D array of sensors.

The resolution of an X-ray image, also called a radiograph, is limited by several factors. The detector used to record the radiograph imposes a fundamental limit on the resolution by fixing the smallest pixel size. Also, detector cross-talk where energy from one sensor pixel leaks into its neighboring sensor pixels [10] causes blur and contrast reduction. Furthermore, the finite non-zero area of the X-ray source aperture manifests as additional blur in the radiograph [11], [12]. Other causes of blur include motion or vibrations in the sample stage or the imaging equipment. Blur is a major detriment in dimensional

metrology applications where it is critical to accurately estimate the relative physical distances between image features. In medical applications, blur hinders the ability to resolve small features such as tumors that may only be a few pixels in size [13]. Hence, mitigating blur is vital to many applications especially when quantitative accuracy is important.

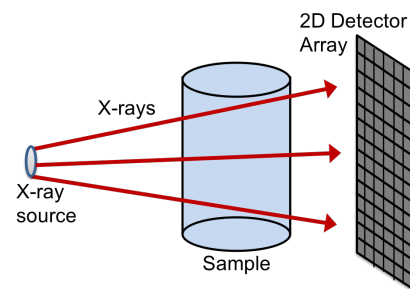


Fig. 1. X-ray imaging experimental setup. An object is exposed to a diverging beam of X-ray radiation and the attenuated X-rays emerging from the object are measured by a flat panel of sensor pixels.

In order to quantify radiographic blur, we use a parametric mathematical model to describe the blurring process. Several papers address the problem of mathematically modeling numerous types of blur such as X-ray source spot blur, detector cross-talk, motion blur, and scatter [11], [14], [15]. A popular strategy is to model blur as a convolution operation with a certain point spread function (PSF). Here, the PSF used to model blur is derived using either simulation [16] or data-driven approaches [17]–[23]. Simulation of PSF relies on precise engineering knowledge of the relevant imaging equipment that may not always be available. Alternatively, data-driven approaches estimate PSF directly from radiographs of known well characterized objects.

Data-driven approaches to blur estimation relies on calculation of the PSF from radiographs of an object with known composition and shape such as a rollbar, slit, pinhole, or other test objects [17]–[21]. However, these methods only estimate one PSF that either models the X-ray source blur, the detector blur, or the total effective blur. They do not address the problem of disentangling and estimating the PSFs of all the different types of blur that simultaneously affect a radiograph. The magnitude of each blur varies depending on the relative placement of the X-ray source, object, and detector. The ability to estimate each individual blur PSF will allow us to predict the radiograph blur for any spatial configuration of X-ray source, object, and detector by appropriately recombining the estimated blur PSFs.

K. A. Mohan is with the Computational Engineering Division (CED) at Lawrence Livermore National Laboratory, Livermore, CA, 94551 USA. E-mail: mohan3@llnl.gov, adityakadri@gmail.com.

R. M. Panas and J. A. Cuadra are with the Materials Engineering Division (MED) at Lawrence Livermore National Laboratory, Livermore, CA, 94551 USA.

Blur in X-ray radiographs can be reduced either by hardware upgrades or using computational algorithms to reduce blur after the experiment. The former approach may not always be feasible due to cost or physical constraints. Alternatively, deblurring algorithms are a cheaper solution to computationally reduce blur in radiographs. The estimated blur PSFs can be used in a wide variety of deblurring algorithms [24]–[29] to reduce blur in radiographs.

In this paper, we present theory and methods to model and characterize the various types of blur in a X-ray imaging system. We apply a systems approach to characterize blur by expressing the PSF of the effective blur in a radiograph as the convolution of multiple blur PSFs with varying origins. Then, we present a numerical optimization algorithm to disentangle and estimate the various blur PSFs from radiographs of a Tungsten plate rollbar. In particular, we focus on the simultaneous estimation of the X-ray source and detector PSFs while assuming negligible motion blur and scatter. Preliminary results using this approach was previously published as an extended abstract [12].

In section II, we present the underlying principles and mathematics of X-ray imaging. We formulate our blur model in section III and estimate its parameters using an optimization algorithm in section IV. In section V, we present two approaches to deblurring radiographs. Finally, results using real experimental data from a Zeiss Xradia Versa X-ray imaging scanner are presented in section VI.

## II. BACKGROUND

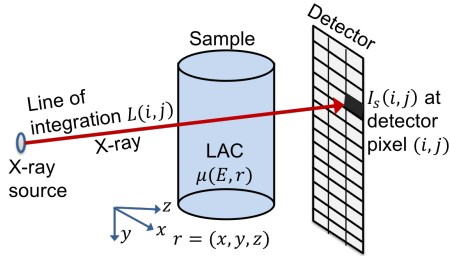


Fig. 2. X-ray propagation model. The detector pixel measurement at location  $(i, j)$  is proportional to the spectrum weighted average of the negative exponential of the integral of the object’s LAC  $\mu(E, r)$  along the line  $L(i, j)$ .

Beer’s law [30] is used to express the magnitude of X-ray attenuation within an object in terms of its thickness and material properties. X-ray attenuation is dependent on a material property called linear attenuation coefficient (LAC) which is a function of the object’s chemical composition, density, and X-ray energy. At detector pixel  $(i, j)$  shown in Fig. 2, according to Beer’s law, the ratio of the X-ray measurement with the object,  $I_s(i, j)$ , and the X-ray measurement without the object,  $I_b(i, j)$ , is given by,

$$\frac{I_s(i, j)}{I_b(i, j)} = \int_E S(E) \exp \left( - \int_{L(i, j)} \mu(E, r) dr \right) dE, \quad (1)$$

where  $\mu(E, r)$  is the LAC of the object at X-ray energy  $E$  and spatial location  $r$ ,  $L(i, j)$  is the line along which  $\mu(E, r)$

is integrated, and  $S(E)$  is the X-ray spectral density such that  $\int_E S(E) dE = 1$  [4]. We will call the expression on the right side of the equality in equation (1) as the ideal transmission function  $\tilde{T}(i, j)$ , i.e.,

$$\tilde{T}(i, j) = \int_E S(E) \exp \left( - \int_{L(i, j)} \mu(E, r) dr \right) dE. \quad (2)$$

The relation in equation (1) is valid in the absence of imaging non-idealities such as noise, blur, and scatter. Dark current is one such non-ideal characteristic where the detector measurements do not drop to zero when there is no X-ray radiation. To compensate for this effect, detector measurements are made without the X-ray beam and subtracted from measurements with the X-ray beam. Detector measurements are also corrupted by electronic noise and photon counting noise that are often modeled as additive Gaussian noise. Let  $I(i, j)$  denote the normalized measurement defined as the ratio of the dark noise corrected measurements with and without the object. If  $I_d(i, j)$  denotes the measurement at detector pixel  $(i, j)$  without X-rays, then,

$$I(i, j) = \frac{I_s(i, j) - I_d(i, j)}{I_b(i, j) - I_d(i, j)} = \tilde{T}(i, j) + w(i, j), \quad (3)$$

where  $w(i, j)$  is Gaussian noise. In the next section, we will modify equation (3) to account for the effects of more non-idealities such as X-ray source blur and detector blur.

The term “radiograph” will henceforth be used to refer to the normalized radiograph i.e.,  $I(i, j)$  over all pixel locations  $(i, j)$ . Also, “bright field” is used to refer to  $I_b(i, j)$  and “dark field” is used to refer to  $I_d(i, j)$ .

## III. FORMULATION OF BLUR MODEL

The effect of various forms of blur on X-ray radiographs is modeled as a linear space-invariant phenomenon. The blur model expresses the radiograph  $I(i, j)$  as the convolution of a transmission function  $T(i, j)$  with multiple two dimensional PSFs each of which models a different form of blur. In the absence of non-idealities such as scatter or temporal drift in values of  $I_b(i, j)$  and  $I_d(i, j)$ , the transmission function  $\tilde{T}(i, j)$  is equal to the ideal transmission function  $\tilde{T}(i, j)$  given in (2). In this paper, we only consider the effect of blur due to X-ray source, detector, and system motion [31].

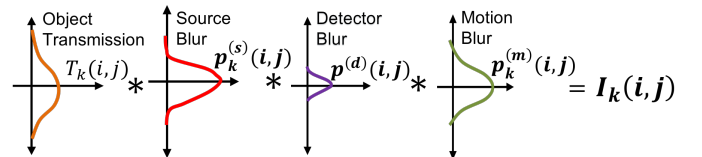


Fig. 3. The measured radiograph is given by the convolution (denoted by  $*$ ) of the transmission function with multiple blur PSFs.

The shape and size of the source and motion PSFs are a function of the X-ray source to object distance (SOD) and object to detector distance (ODD). Since detector blur is due to cross-talk between detector pixels, it does not vary with SOD and ODD. Let  $p_k^{(s)}(i, j)$  and  $p_k^{(m)}(i, j)$  denote the PSFs

of the X-ray source blur and motion blur respectively at a SOD of  $SOD_k$  and ODD of  $ODD_k$ . Based on the analysis in [32]–[34], we will approximate the motion PSF as a Kronecker delta function since its full width half maximum (FWHM) was determined to be much smaller than our detector pixel size. If  $I_k(i, j)$  is the radiograph and  $T_k(i, j)$  is the transmission function at a SOD of  $SOD_k$  and ODD of  $ODD_k$ , then,

$$I_k(i, j) = T_k(i, j) * p_k^{(s)}(i, j) * p^{(d)}(i, j) * p_k^{(m)}(i, j), \quad (4)$$

where  $*$  denotes 2D convolution (Fig. 3). Using equation (4), our goal is to estimate the PSFs of X-ray source and detector blur given the radiographs  $I_k(i, j)$  at various SOD and ODD.

### A. Transmission Function

Simultaneous estimation of the transmission function,  $T_k(i, j)$ , and the blur PSFs,  $p_k^{(s)}(i, j)$  and  $p^{(d)}(i, j)$ , is an ill-posed problem. Hence, we scan a object with known dimensions and chemical composition. Since our object is known, we can compute the ideal transmission function  $\tilde{T}_k(i, j)$  for each scan (indexed by  $k$ ) using equation (2). The transmission function  $T_k(i, j)$  is then modeled as an affine transformation of the ideal transmission function  $\tilde{T}_k(i, j)$  such that

$$T_k(i, j) = l_k + (h_k - l_k)\tilde{T}_k(i, j), \quad (5)$$

where  $l_k$  and  $h_k$  are scalars. The parameters  $l_k$  and  $h_k$  are used to compensate for uniform shifts in the measured X-ray intensity due to non-idealities such as drift in the values of  $I_b(i, j)$  and  $I_d(i, j)$  over time, inaccuracies in the calculation of  $\tilde{T}_k(i, j)$ , and low-frequency effects such as scatter. Temporal drifts in  $I_b(i, j)$  and  $I_d(i, j)$  can occur if there is any change in dark current or X-ray source intensity.



Fig. 4. (a) Tungsten plate rollbar mounted in a sample holder. (b) Tungsten plate placed in between the X-ray source and detector such that its top rolled edge appears as a horizontal edge in the radiograph.

For our experiments, we fabricated a Tungsten plate with a sharp edge and uniform thickness that is sufficient to block all incoming X-rays (Fig. 4). The plate is then exposed to X-rays such that the sharp edge passes through the center of the radiograph as shown in Fig. 5 (a). The plane of the Tungsten plate is aligned such that it is perpendicular to the direction of X-ray propagation. Since perfect alignment is very challenging, the sharp edges are rolled [19] to one meter radius of curvature, which permits alignment errors of up to one degree. Fig. 5 (b) shows the ideal transmission function for the radiograph in Fig. 5 (a). The procedure used to compute the ideal transmission function is presented in Appendix A.

Due to scatter and variations in  $I_b(i, j)$  and  $I_d(i, j)$ ,  $T_k(i, j)$  is not the same as  $\tilde{T}_k(i, j)$ . The values of  $l_k$  and  $h_k$  that determine the relation between  $T_k(i, j)$  and  $\tilde{T}_k(i, j)$  in (5)

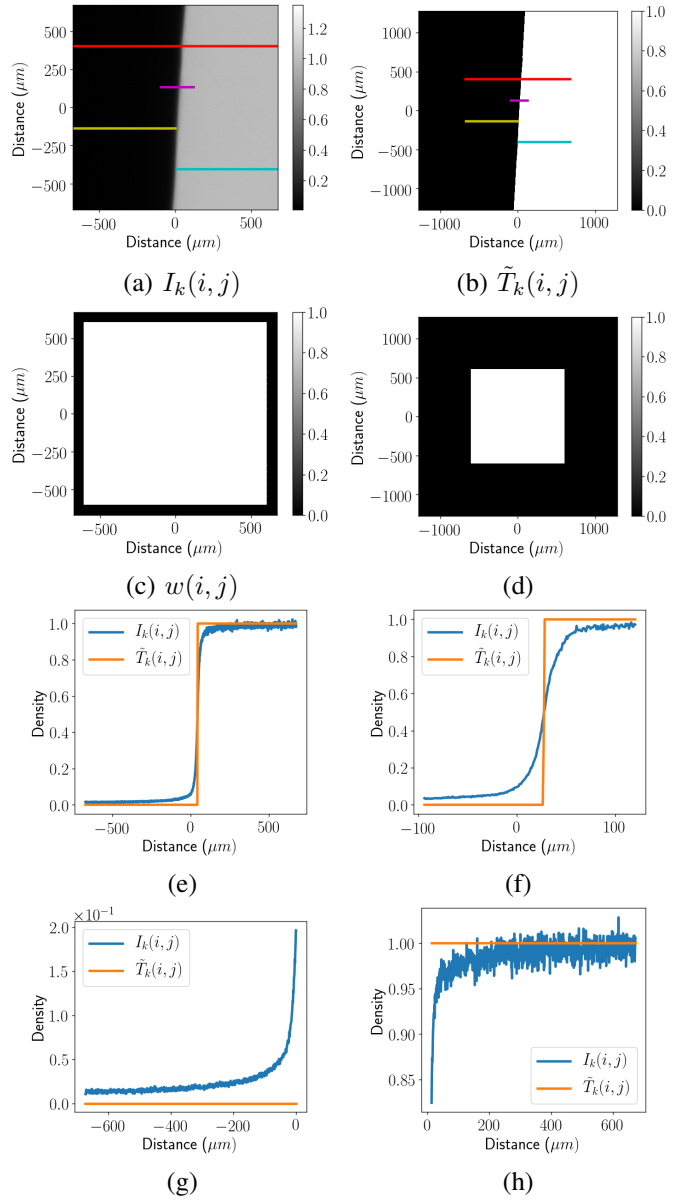


Fig. 5. (a) Radiograph  $I_k(i, j)$  of a Tungsten sharp edge. (b) Padded ideal transmission function  $\tilde{T}_k(i, j)$  that is derived from (a). The bright regions in (c) and (d) indicate the regions of (a) and (b) respectively that is included in the optimization of equation (6). The origin  $(0, 0)$  is at the center of all images (a-d). The bright regions in (c) and (d) have the same number of pixels and same pixel width. The width of the image in (d) is greater than (c) due to additional padding in (d). (e), (f), (g), and (h) are line profile plots along the colored lines in images (a) and (b).

are jointly estimated during the blur estimation procedure that will be presented in the next section. However, to aid this procedure, we have to supply initial estimates for  $l_k$  and  $h_k$  that are determined by solving the following least squares problem,

$$\begin{aligned} (\hat{l}_k, \hat{h}_k) &= \arg \min_{l_k, h_k} \frac{1}{2} \sum_{i, j} w(i, j) (I_k(i, j) - T_k(i, j))^2 \\ &\text{where } T_k(i, j) = l_k + (h_k - l_k)\tilde{T}_k(i, j), \end{aligned} \quad (6)$$

where  $w(i, j)$  is the weight term that is 0 for pixels that are close to the boundaries of the image  $I_k(i, j)$  and 1 elsewhere

(Fig. (5) (c)). The padded region of  $\tilde{T}(i, j)$  is also excluded from the least squares (Fig. (5) (d)). The solution to (6) is,

$$\begin{pmatrix} \hat{i}_k \\ \hat{h}_k \end{pmatrix} = H_k^{-1} \left( \sum_{i,j} w(i, j) \begin{pmatrix} I_k(i, j) (1 - \tilde{T}_k(i, j)) \\ I_k(i, j) \tilde{T}_k(i, j) \end{pmatrix} \right), \quad (7)$$

where  $H_k =$

$$\sum_{i,j} w(i, j) \begin{pmatrix} 1 - 2\tilde{T}_k(i, j) + \tilde{T}_k^2(i, j) & \tilde{T}_k(i, j) - \tilde{T}_k^2(i, j) \\ \tilde{T}_k(i, j) - \tilde{T}_k^2(i, j) & \tilde{T}_k^2(i, j) \end{pmatrix}.$$

### B. Source Blur

The PSF of source blur is mathematically modeled using a 2D exponential density function. This function is parameterized by two scale parameters  $s_{sx}$  and  $s_{sy}$  that are a measure of the spatial width of the PSF along the  $x$ -axis and  $y$ -axis in the plane of the X-ray source. The scale parameters are related to the full width half maximums (FWHM) along the  $x$ -axis as  $W_{sx} = -2 \log(0.5)/s_{sx}$  and along the  $y$ -axis as  $W_{sy} = -2 \log(0.5)/s_{sy}$ . By definition, FWHM  $W_{sx}$  is the distance between two points along the  $x$ -axis where the PSF drops to half of its maximum value and FWHM  $W_{sy}$  is the corresponding distance along the  $y$ -axis. If  $\Delta$  denotes the width of each pixel, the PSF of source blur in the plane of the X-ray source is modeled as,

$$p^{(s)}(i, j) = \frac{1}{Z_s} \exp\left(-\Delta \sqrt{s_{sx}^2 i^2 + s_{sy}^2 j^2}\right), \quad (8)$$

where  $Z_s$  is the normalizing constant given by

$$Z_s = \sum_i \sum_j \exp\left(-\Delta \sqrt{s_{sx}^2 i^2 + s_{sy}^2 j^2}\right). \quad (9)$$

The constant  $Z_s$  ensures that  $p^{(s)}(i, j)$  sums to one when summed over all  $(i, j)$ .

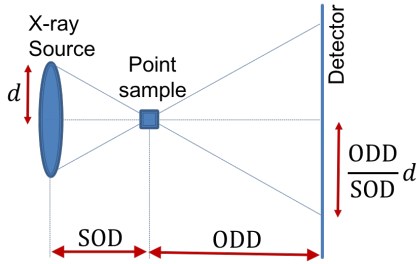


Fig. 6. The width of source blur on the detector plane is directly proportional to the object to detector distance (ODD) and inversely proportional to the source to object distance (SOD).

At the detector plane, the FWHM of source blur is scaled by a factor of ODD/SOD. The change in FWHM of source blur with varying ODD and SOD is depicted in Fig. 6. For the  $k^{th}$  radiograph, the PSF of source blur on the detector plane is given by,

$$p_k^{(s)}(i, j) = \frac{1}{Z_{s,k}} \exp\left(-\frac{SOD_k}{ODD_k} \Delta \sqrt{s_{sx}^2 i^2 + s_{sy}^2 j^2}\right), \quad (10)$$

where  $Z_{s,k}$  is the normalizing constant given by

$$Z_{s,k} = \sum_i \sum_j \exp\left(-\frac{SOD_k}{ODD_k} \Delta \sqrt{s_{sx}^2 i^2 + s_{sy}^2 j^2}\right). \quad (11)$$

### C. Detector Blur

The detector blur is modeled using a mixture of two exponential density functions with scale parameters  $s_{d1}$  and  $s_{d2}$ . If  $p^{(d)}(i, j)$  denotes the PSF of detector blur, then,

$$p^{(d)}(i, j) = q \frac{1}{Z_{d1}} \exp\left(-s_{d1} \Delta \sqrt{i^2 + j^2}\right) + (1 - q) \frac{1}{Z_{d2}} \exp\left(-s_{d2} \Delta \sqrt{i^2 + j^2}\right) \quad (12)$$

where  $q$  is the mixture parameter and  $Z_{d1}, Z_{d2}$  are normalizing constants such that

$$Z_{d1} = \sum_i \sum_j \exp\left(-s_{d1} \Delta \sqrt{i^2 + j^2}\right) \quad (13)$$

$$Z_{d2} = \sum_i \sum_j \exp\left(-s_{d2} \Delta \sqrt{i^2 + j^2}\right). \quad (14)$$

Also,  $q$  and  $1 - q$  are parameters that function as weights for the two exponentials. The scale parameters are related to the FWHMs of the two exponential functions in (12) as  $W_{d1} = -2 \log(0.5)/s_{d1}$  and  $W_{d2} = -2 \log(0.5)/s_{d2}$ .

In our experiments, we expect the detector PSF to be dominated by the first exponential with a large weight of  $q \approx 0.9$  and a very small FWHM  $W_{d1}$  that spans only a few pixels. The second exponential is expected to have a smaller weight of  $1 - q \approx 0.1$  and a very large FWHM  $W_{d2}$  that spans several hundreds of pixels. Depending on the X-ray imaging system, the values for  $W_{d1}, W_{d2}$  and  $q$  may change but (12) is still expected to be a good model for detector PSF.

### D. Motion Blur

An additional source of blur is the relative motion of all components in the X-ray system. If these components move during the data acquisition period, then they will result in motion of the object's image on the detector surface. Such motion will distribute the apparent location of an edge or feature over a range of locations, appearing to blur it in a manner that can be captured with a motion PSF that is convolved with the image. The system motion is calculated via a geometric analysis of the relative locations of components, propagated to the detector screen. This is done using an uncertainty propagation model presented in [32]–[34]. Motion blur is denoted by  $p_k^{(m)}(i, j)$  and is typically modeled as a Gaussian density function. This form of blur also depends on the relative positions of X-ray source, object, and detector. However, we will approximate the motion PSF as a Kronecker delta function since its FWHM was determined to be much smaller than the detector pixel size in our experiments.



#### IV. ESTIMATION OF BLUR MODEL

Blur model estimation is the process of estimating all the parameters  $s_{sx}, s_{sy}, s_{d1}, s_{d2}$ , and  $q$  of the PSFs given known values for  $I_k(i, j)$  and  $T_k(i, j)$  in equations (4) and (5). We will only estimate  $p_k^{(s)}(i, j)$  and  $p^{(d)}(i, j)$  in (4) since  $p_k^{(m)}(i, j)$  is assumed to be a constant delta function. By constraining  $p_k^{(s)}(i, j)$  to take the shape of the exponential density function in (8) and  $p^{(d)}(i, j)$  to take the shape of the exponential mixture density function in (12), blur estimation reduces to the problem of estimating the parameters  $s_{sx}, s_{sy}, s_{d1}, s_{d2}$ , and  $q$ . For every  $k^{th}$  radiograph, the parameters  $l_k$  and  $h_k$  in (5) are also treated as unknowns and jointly estimated along with the PSF parameters.

Note that the form of source PSF as evaluated on the detector plane given by (10) depends on the ratio of the object to detector distance  $ODD_k$  and the source to object distance  $SOD_k$ . Thus, while the amount of source blur in the radiograph  $I_k(i, j)$  is a function of  $ODD_k$  and  $SOD_k$ , the detector blur does not change with  $ODD_k$  and  $SOD_k$ . To estimate both source and detector PSF parameters, it is necessary to acquire radiographs at a minimum of two different values of  $ODD_k/SOD_k$ . Also, since the source PSF has two scale parameters modeling the width along  $x$ -axis and  $y$ -axis, we need radiographs for cases when the Tungsten edge is horizontal and vertical.

We use numerical optimization to estimate all blur and transmission parameters given radiographs at different values of ODD and SOD. The parameters are estimated by solving,

$$\left( \begin{array}{c} \hat{s}_{sx}, \hat{s}_{sy}, \hat{s}_{d1}, \hat{s}_{d2}, \hat{q}, \\ \hat{l}_1, \dots, \hat{l}_K, \hat{h}_1, \dots, \hat{h}_K \end{array} \right) = \arg \min_{\substack{s_{sx}, s_{sy}, s_{d1}, s_{d2}, q \\ l_1, \dots, l_K, h_1, \dots, h_K}} \sum_{k=1}^K E_k \quad (15)$$

$$\begin{aligned} \text{where } E_k &= 0.5 \sum_{i,j} w_k(i, j) (I_k(i, j) - \\ & T_k(i, j) * p_k^{(s)}(i, j) * p^{(d)}(i, j) * p_k^{(m)}(i, j))^2, \\ \text{subject to } & s_{sx} \geq 0, s_{sy} \geq 0, s_{d1} \geq 0, s_{d2} \geq 0, \\ & 0.8 \leq q \leq 1, -1 \leq l_k \leq 0.5, 0.5 \leq h_k \leq 2, \end{aligned} \quad (16)$$

where  $K$  is the total number of radiographs. The parameters  $\hat{s}_{sx}, \hat{s}_{sy}, \hat{s}_{d1}, \hat{s}_{d2}, \hat{q}, \hat{l}_k$ , and  $\hat{h}_k, \forall k$  are the estimated values of  $s_{sx}, s_{sy}, s_{d1}, s_{d2}, q, l_k$  and  $h_k, \forall k$  respectively. The lower bound of 0.8 for  $q$  ensures that the first exponential in (12) is chosen to have the largest weight.

We solve the minimization problem in (15) using the L-BFGS-B algorithm [35]. L-BFGS-B is a quasi-Newton method for solving optimization problems and requires information of the gradient of the objective function,  $\sum_{k=1}^K E_k$ , with respect to all the variables being optimized. It also supports bound constraints on each of the variables that are optimized. However, since the optimization problem in (15) is non-convex, the optimized variables may be stuck in a local minima or a saddle point. Thus, good initialization of each variable is necessary before running L-BFGS-B to ensure reliable convergence to a solution that best fits the measured radiographs. Our approach

---

#### Algorithm 1 Blur Estimation Algorithm

---

- 1: Estimation of  $s_{sx}$  and  $s_{sy}$  from  $K/2$  number of radiographs with the highest  $ODD_k/SOD_k$ . Let  $\Omega_s$  be the set of all indices of these radiographs. Parameters  $l_k$  and  $h_k$  for all  $k \in \Omega_s$  are initialized using (7).

$$(\hat{s}_{sx}, \hat{s}_{sy}) = \arg \min_{s_{sx} \geq 0, s_{sy} \geq 0} \sum_{k \in \Omega_s} E_k. \quad (17)$$

- 2: Estimation of  $s_{d1}, s_{d2}$ , and  $q$  from  $K/2$  number of radiographs with the lowest  $ODD_k/SOD_k$ . Let  $\Omega_d$  be the set of all indices of these radiographs. Parameters  $l_k$  and  $h_k$  for all  $k \in \Omega_d$  are initialized using (7).

$$(\hat{s}_{d1}, \hat{s}_{d2}, \hat{q}) = \arg \min_{s_{d1} \geq 0, s_{d2} \geq 0, 0.8 \leq q \leq 1} \sum_{k \in \Omega_d} E_k \quad (18)$$

- 3: Estimation of all parameters  $s_{sx}, s_{sy}, s_{d1}, s_{d2}, q, l_k$ , and  $h_k$ .  $s_{sx}$  and  $s_{sy}$  are initialized with the estimated values  $\hat{s}_{sx}$  and  $\hat{s}_{sy}$  from step 1.  $s_{d1}, s_{d2}$ , and  $q$  are initialized with the estimated values  $\hat{s}_{d1}, \hat{s}_{d2}$ , and  $\hat{q}$  from step 2.  $l_k$  and  $h_k$  are initialized using (7) for all  $k$ .

$$\left( \begin{array}{c} \hat{s}_{sx}, \hat{s}_{sy}, \hat{s}_{d1}, \hat{s}_{d2}, \hat{q}, \\ \hat{l}_1, \dots, \hat{l}_K, \hat{h}_1, \dots, \hat{h}_K \end{array} \right) = \arg \min_{\substack{s_{sx}, s_{sy}, s_{d1}, s_{d2}, q \\ l_1, \dots, l_K, h_1, \dots, h_K}} \sum_{k=1}^K E_k$$

subject to constraints in (16). (19)

---

to solving (15) is outlined in algorithm 1. We use the L-BFGS-B implementation in the python package *scipy* [36], [37]. The gradients that must be supplied to the L-BFGS-B algorithm are derived in Appendix B.

In algorithm 1, steps 1 and 2 are used to produce good initial estimates of the source and detector PSF parameters for initializing the optimization in step 3. In step 1, only source PSF parameters are estimated from half of all radiographs with the highest  $ODD_k/SOD_k$  where source blur is significant if not dominant. In step 2, only detector PSF parameters are estimated from half of all radiographs with the lowest  $ODD_k/SOD_k$  where detector blur is significant if not dominant. In step 3, all parameters from the source PSF, detector PSF, and transmission function are jointly optimized to arrive at the final estimates.

#### V. DEBLURRING ALGORITHMS

Deblurring is the process of reducing blur in radiographs using computational algorithms. We focus on using Wiener filter [25], [28] and regularized least squares deconvolution [26]–[28] for deblurring radiographs. These algorithms take as input the convolution of all PSFs given by,

$$\hat{p}_k(i, j) = \hat{p}_k^{(s)}(i, j) * \hat{p}^{(d)}(i, j) * \hat{p}_k^{(m)}(i, j), \quad (20)$$

which is a function of the source to object distance  $SOD_k$  and object to detector distance  $ODD_k$  of the input radiograph  $I_k(i, j)$ . In (20),  $\hat{p}_k^{(s)}(i, j)$  and  $\hat{p}^{(d)}(i, j)$  are obtained by substituting the estimated values  $\hat{s}_{sx}, \hat{s}_{sy}, \hat{s}_{d1}, \hat{s}_{d2}$ , and  $\hat{q}$  from step 3 of algorithm 1 in equations (10) and (12). The PSF

$\hat{p}_k^{(m)}(i, j)$  is assumed to be a delta function since FWHM of motion blur was determined to be much smaller than the pixel width using the analysis in [32]–[34].

#### A. Wiener Filter

Wiener filter [25], [28] reduces blur by deconvolving the convolution of all PSFs,  $\hat{p}_k(i, j)$  in (20), from the blurred radiograph. Deconvolution is implemented in Fourier space by dividing the Fourier transform of the radiograph with the Fourier transform of the PSFs. To reduce noise, regularization is used to enforce smoothness. We use the function *skimage.restoration.wiener* in the python package [38] that implements the method in [25].

#### B. Regularized Least Squares Deconvolution (RLSD)

In RLSD [26]–[28], [39], we solve the following optimization problem to deblur a radiograph  $I_k(i, j)$ ,

$$\hat{T}_k(i, j) = \arg \min_{T_k(i, j), \forall i, j} \left\{ \sum_{i, j} w_k(i, j) (I_k(i, j) - T_k(i, j) * \hat{p}_k(i, j))^2 + \beta \sum_{((i, j), (m, n)) \in \mathcal{N}} \tilde{w}(i, j, m, n) |T_k(i, j) - T_k(m, n)|^{1.2} \right\}, \quad (21)$$

where  $\hat{T}_k(i, j)$  is the deblurred radiograph,  $\beta$  is the regularization parameter, the regularization weight parameter  $\tilde{w}(i, j, m, n) = \frac{1}{\sqrt{(i-m)^2 + (j-n)^2}}$  is inversely proportional to the distance between neighboring pixels, and  $\mathcal{N}$  is the set of all pairs of neighboring pixel indices i.e.,  $((i, j), (m, n)) \in \mathcal{N}$  if pixel  $(m, n)$  lies within a  $3 \times 3$  neighborhood of pixel  $(i, j)$ . For simplicity, the weight parameter  $w_k(i, j)$  is chosen to be 1 for all  $(i, j)$  in our experiments. Ideally,  $w_k(i, j)$  should be set such that it is inversely proportional to the variance of noise in  $I_k(i, j)$ .

The regularization function in (21) enforces smoothness in  $T_k(i, j)$  by penalizing the difference in values between neighboring pixels with a 1.2-norm penalty function [39], [40]. The optimization problem in (21) is solved using the L-BFGS-B algorithm [35].

## VI. RESULTS

In this section, we will estimate the blur model for a Zeiss Xradia 510 Versa X-ray imaging system. After estimating the blur model, we use Wiener filtering and RLSD (described in section V) to deblur radiographs of a star shaped test object that is composed of a  $1\mu\text{m}$  thick Tungsten layer on a SiN membrane.

The Versa is a commercial micro-CT system that consists of a transmissive X-ray tube with a Tungsten target anode that exhibits bremsstrahlung X-ray spectral characteristics. The accelerating voltage was selected to be  $160\text{kV}$  and the tube current was  $62.5\mu\text{A}$ . This resulted in an average flux of  $1.37 \times 10^{11} \text{ counts } \text{m}^{-2} \text{ nstr}^{-1} \text{ sec}^{-1}$ . The detector consists of an optically coupled Thallium-doped Cesium Iodide scintillator

and a  $5\text{MP}$  CCD with a  $13.5\mu\text{m}$  pixel size, 16-bit depth, and a maximum dark current noise of about  $12 \text{ counts } \text{sec}^{-1}$ . Bright field images (radiographs without object)  $I_b(i, j)$  and dark field images (radiographs with X-rays off)  $I_d(i, j)$  were acquired to appropriately normalize each radiograph image of the object using equation (3). All radiographs were acquired using a  $20\times$  magnification lens resulting in an effective pixel size of  $\Delta = 0.675\mu\text{m}$ .

#### A. Blur Parameter Estimation

Radiographs of a Tungsten plate rollbar are used to estimate the blur model parameters  $s_{sx}, s_{sy}, s_{d1}, s_{d2}$ , and  $q$  by solving the optimization problem in equation (15). The source to detector distance (SDD) for all radiographs was fixed at  $71\text{mm}$ . First, the Tungsten plate edge is oriented in the vertical direction (Fig. 5 (a)) and radiographs are acquired at source to object distances (SOD) of  $13\text{mm}, 24.8\text{mm}, 37.5\text{mm}, 50.3\text{mm}$ , and  $60\text{mm}$ . Next, the edge is oriented in the horizontal direction and radiographs are acquired at SOD of  $12\text{mm}, 24.8\text{mm}, 37.5\text{mm}$ , and  $65.3\text{mm}$ . Since SDD is  $71\text{mm}$ , the ODD for each radiograph is given by  $(71 - \text{SOD})\text{mm}$ . For each radiograph, the Tungsten plate is oriented such that its edge is slightly tilted away from the horizontal or vertical directions as shown in Fig. 5 (a). This is done to ensure that the Tungsten edge is never exactly parallel to a row or column of detector pixels.

The traditional approach to estimating X-ray source parameters is to use one horizontal and one vertical edge radiograph while assuming there is no detector blur. To evaluate this approach, we estimate source parameters by solving (17) using a single set of horizontal and vertical edge radiographs. In (17), we do not estimate the transmission function parameters  $(l_k, h_k)$ . The estimated values of X-ray source parameters for various source to object distances (SOD) are shown in table I. Since FWHMs ( $W_{sx}, W_{sy}$ ) are more easily interpretable than scale parameters ( $s_{sx}, s_{sy}$ ), we show the FWHMs instead of the scale parameters. We see that the estimated values for the FWHMs consistently increase with increasing values of SOD in table I since the source FWHMs were estimated while assuming there is no detector blur. Hence, the detector blur in the input radiographs get interpreted as X-ray source blur, which causes the X-ray source FWHMs to increase by a factor of SOD/ODD times the FWHM of detector blur.

The traditional approach to detector blur estimation is to use one horizontal and one vertical edge radiograph while assuming there is no source blur. To evaluate this approach,

TABLE I  
FWHMs  $W_{sx}$  AND  $W_{sy}$  OF THE X-RAY SOURCE PSF ESTIMATED USING ONE SET OF HORIZONTAL AND VERTICAL EDGE RADIOGRAPHS.

horizontal SOD (mm)	vertical SOD (mm)	$W_{sx}$ ( $\mu\text{m}$ )	$W_{sy}$ ( $\mu\text{m}$ )
12.0	13.0	3.13	3.52
24.8	24.8	3.53	3.87
37.5	37.5	4.47	4.57
50.3	50.3	6.76	6.85
65.3	60.0	12.83	25.86

TABLE II  
PARAMETERS  $q$ ,  $W_{d1}$ , AND  $W_{d2}$  OF THE DETECTOR PSF ESTIMATED USING ONE SET OF HORIZONTAL AND VERTICAL EDGE RADIOGRAPHS.

horizontal SOD (mm)	vertical SOD (mm)	$W_{d1}$ ( $\mu\text{m}$ )	$W_{d2}$ ( $\mu\text{m}$ )	$q$
12.0	13.0	11.79	62.1	0.85
24.8	24.8	5.43	62.5	0.90
37.5	37.5	3.27	68.4	0.92
50.3	50.3	2.25	63.1	0.92
65.3	60.0	1.83	54.3	0.92

TABLE III  
X-RAY SOURCE AND DETECTOR PARAMETERS ESTIMATED USING TWO SETS OF HORIZONTAL AND VERTICAL EDGE RADIOGRAPHS.

horizontal SOD (mm)	vertical SOD (mm)	$W_{sx}$ ( $\mu\text{m}$ )	$W_{sy}$ ( $\mu\text{m}$ )	$W_{d1}$ ( $\mu\text{m}$ )	$W_{d2}$ ( $\mu\text{m}$ )	$q$
12.0, 24.8	13.0, 24.8	2.59	2.96	1.55	129.6	0.90
12.0, 37.5	13.0, 37.5	2.61	2.98	1.90	145.7	0.91
12.0, 50.3	13.0, 50.3	2.61	3.00	1.86	137.9	0.91
12.0, 65.3	13.0, 60.0	2.65	3.05	1.82	143.2	0.92
24.8, 37.5	24.8, 37.5	2.70	2.98	1.86	129.8	0.91
24.8, 50.3	24.8, 50.3	2.58	2.96	1.97	120.3	0.92
24.8, 65.3	24.8, 60.0	2.73	3.05	1.82	119.5	0.92
37.5, 50.3	37.5, 50.3	2.81	2.96	1.90	127.8	0.92
37.5, 65.3	37.5, 60.0	2.92	3.06	1.85	127.2	0.93
50.3, 65.3	50.3, 60.0	2.88	2.95	1.87	113.1	0.93

TABLE IV  
MEAN AND STANDARD DEVIATION OF PARAMETERS ESTIMATED USING TWO SETS OF HORIZONTAL AND VERTICAL EDGE RADIOGRAPHS.

	$W_{sx}$ ( $\mu\text{m}$ )	$W_{sy}$ ( $\mu\text{m}$ )	$W_{d1}$ ( $\mu\text{m}$ )	$W_{d2}$ ( $\mu\text{m}$ )	$q$
mean	2.71	2.99	1.84	129.4	0.92
variance	0.12	0.04	0.11	9.9	0.01

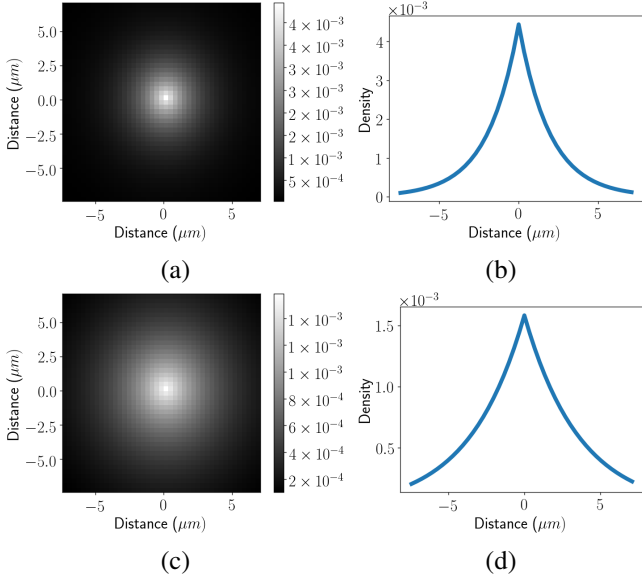


Fig. 7. (a) X-ray source PSF in the source plane obtained by substituting the mean values of table IV in equation (8). (b) X-ray source PSF in the detector plane for a SOD of 24.8mm and ODD of 46.2mm by substituting the mean values of table IV in equation (10). (c) and (d) are line profile plots along a horizontal line through the center of the images in (a) and (c) respectively.

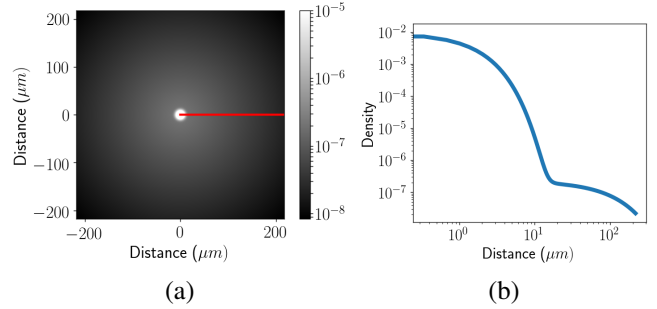


Fig. 8. (a) Detector PSF in logarithmic space obtained by substituting the mean values of table IV in equation (12). (b) Line profile plot along a horizontal line through the center of the image in (a).

TABLE V  
ESTIMATED PARAMETERS BEFORE AND AFTER STEP (3) OF ALGORITHM 1 USING HORIZONTAL RADIOGRAPHS AT SOD OF 50mm, 65mm AND VERTICAL RADIOGRAPHS AT SOD OF 50mm, 60mm.

	$W_{sx}$ ( $\mu\text{m}$ )	$W_{sy}$ ( $\mu\text{m}$ )	$W_{d1}$ ( $\mu\text{m}$ )	$W_{d2}$ ( $\mu\text{m}$ )	$q$
Before step (3)	6.76	6.85	1.83	54.35	0.92
After step (3)	2.88	2.95	1.87	113.05	0.93

we estimate detector PSF parameters by solving (18) using a single set of horizontal and vertical edge radiographs. The estimated parameters of detector blur are shown in table II. In (18), we do not estimate  $(l_k, h_k)$ . In this case, we see that the estimated value for FWHM  $W_{d1}$  decreases with increasing SOD since we assumed that there is no X-ray source blur. Note that the first exponential with FWHM of  $W_{d1}$  in (12) is dominant since its weight given by  $q$  is approximately 0.9 in table II. As SOD increases and ODD decreases, the FWHM of the source blur on the detector plane reduces. However, since source blur is interpreted as detector blur, the estimated FWHM  $W_{d1}$  also decreases as SOD is increased. In contrast,  $W_{d2}$  and  $q$  do not seem to have a significant dependence on SOD.

Next, we use horizontal edge radiographs at two SODs and vertical edge radiographs at two SODs to simultaneously estimate both source and detector blur parameters using algorithm 1. The estimated values of blur parameters after step 3 of algorithm 1 are shown in table III. In this case, the estimation of X-ray source and detector parameters are stable without any noticeable dependence on SOD. The mean and standard deviation of the estimated parameters computed across various SODs (mean of last five columns in table III) are shown in table IV. By simultaneously accounting for both the X-ray source and detector blur, we are able to perform stable estimation of all PSF parameters. We can also see that  $W_{d2}$  is significantly larger in table III than in table II. This increase in  $W_{d2}$  is due to the simultaneous estimation of  $(l_k, h_k)$  of the transmission function along with  $W_{d2}$  of detector blur in step 3 of algorithm 1. To obtain a better fit, the optimizer decreases  $l_k$ , increases  $h_k$ , which in turn allows for  $W_{d2}$  to increase. Since  $W_{d2}$  models the long tails of the detector PSF in (12), it is most sensitive to changes in  $l_k$  and  $h_k$ . In our experiments, we have noticed that the other blur parameters

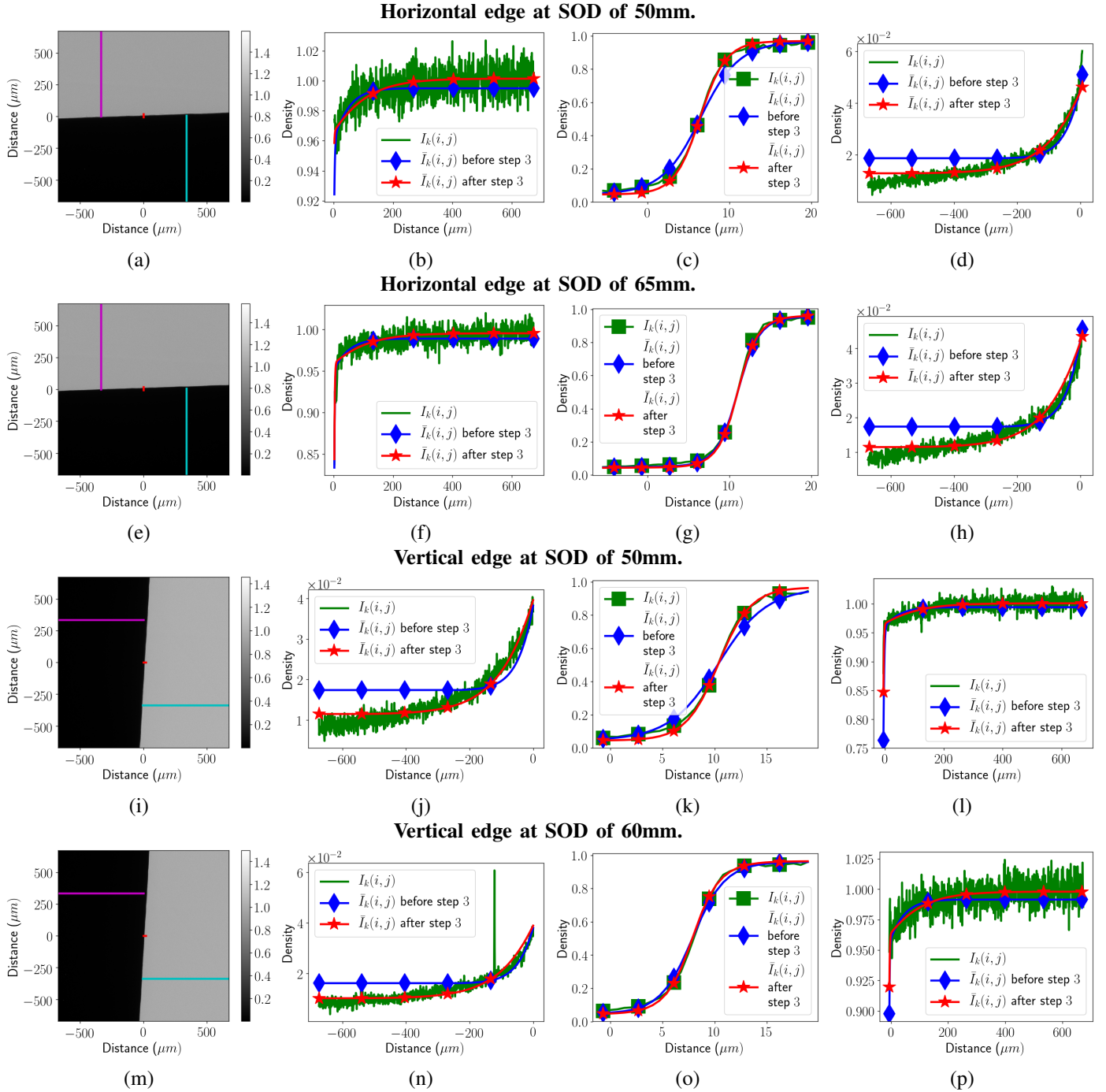


Fig. 9. Agreement between estimated blur and observed experimental blur in radiographs. (a,e,i,m) show the radiographs that were used to estimate blur parameters. (b-d), (f-h), (j-l), and (n-p) are line profile plots demonstrating the agreement between the blur in the measured radiograph  $I_k(i, j)$  and the estimated radiograph  $\bar{I}_k(i, j) = T_k(i, j) * p_k^{(s)}(i, j) * p_k^{(d)}(i, j) * p_k^{(m)}(i, j)$ . The plots in (b,f,j,n), (c,g,k,o), and (d,h,l,p) are along the magenta, red, and cyan colored lines in (a,e,i,m) respectively. We can see that the accuracy of fit improves after step (3) of algorithm 1.

do not have a significant dependence on the values of  $l_k$  and  $h_k$ .

The source PSF as evaluated in the plane of the source and detector are shown in Fig. 7. The PSF is obtained by substituting the mean values of  $W_{sx}$  and  $W_{sy}$  shown in table IV in equations (8) and (10). Since  $W_{sx}$  and  $W_{sy}$  are approximately the same, we can conclude that the source PSF is approximately circular in shape. Using the method in [21],

the manufacturer of the X-ray system estimated the source PSF to have a FWHM of  $3.63\mu\text{m}$  using calibration data at a SOD of  $10\text{mm}$  and ODD of  $30\text{mm}$ . Thus, the ratio ODD/SOD lies in between the data acquisition parameters of the first and second rows in table I. Since the manufacturer's estimate did not account for detector blur, their values are a good match with our estimates that also ignore detector blur.

The detector PSF is shown in Fig. 8 and is evaluated by



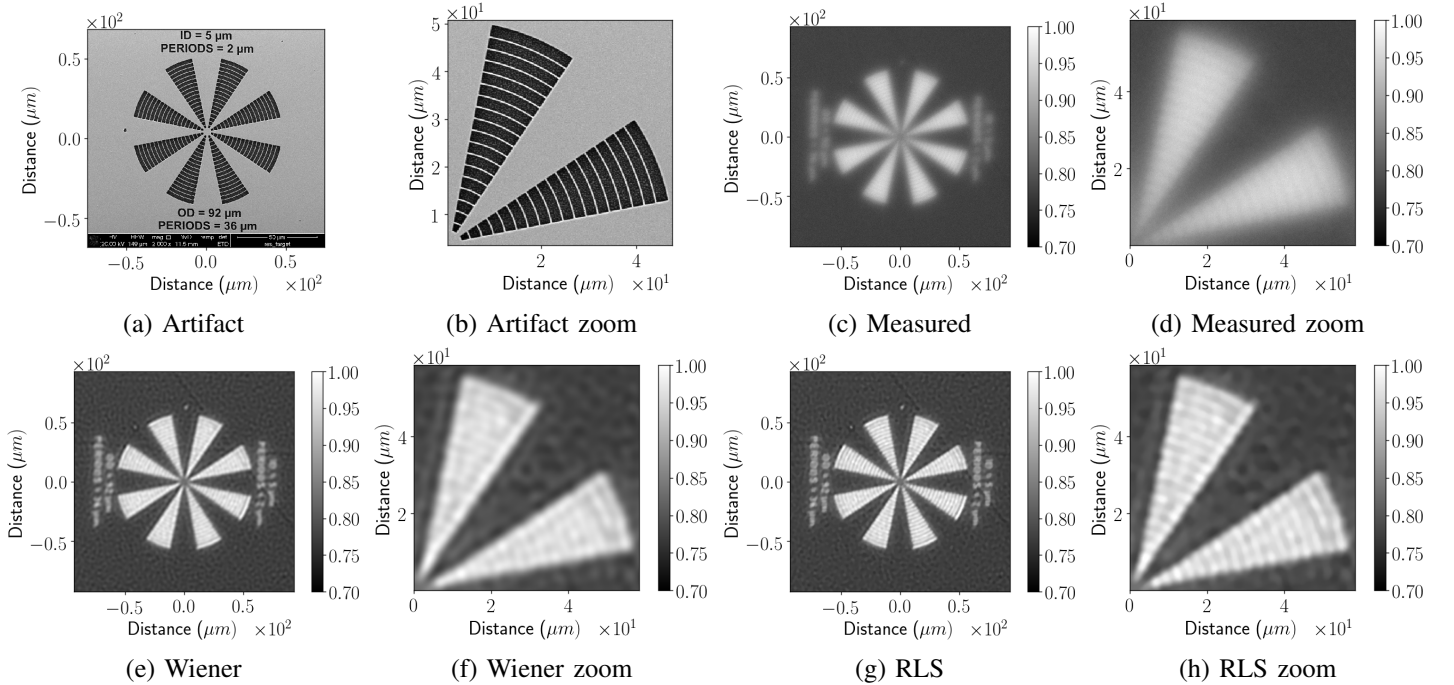


Fig. 10. Deblurring radiographs of a star shaped pattern. (a) shows a star shaped artifact imaged using scanning electron microscopy (SEM). (c) shows the X-ray radiograph of the artifact. (e) shows the X-ray radiograph that is deblurred using Wiener filtering with a regularization of 5.4. (g) shows the X-ray radiograph that is deblurred using RLS with a regularization of 0.0008. (b), (d), (f), and (h) zooms into the top right corner of the images in (a), (c), (e), and (g) respectively. Both Wiener filtering and RLS reduce blur. RLS better preserves sharpness when compared to Wiener filtering.

substituting the mean values of  $W_{d1}$ ,  $W_{d2}$ , and  $q$  shown in table IV in equation (12). Since the FWHM  $W_{d1}$  of the first exponential density in (12) with the high weight  $q$  is only a few pixels wide (pixel width being  $0.675\mu\text{m}$ ), we can deduce that most of the detector blur is limited to only a few pixels. Alternatively, the large value of FWHM  $W_{d2}$  of the second exponential density with a smaller weight of  $(1 - q)$  suggests that there is significant leakage of electric charge all the way to the corners of the detector array.

Table V and Fig. 9 validate the necessity to simultaneously optimize the source blur, detector blur, and transmission function. While step 1 and step 2 of algorithm 1 independently estimate source and detector blur, step 3 estimate both forms of blur simultaneously. The estimated parameters before and after step (3) of algorithm 1 are shown in table V. Fig. 9 shows line profile plots that compare the input radiograph  $I_k(i, j)$  with the prediction estimate  $\bar{I}_k(i, j) = T_k(i, j) * p_k^{(s)}(i, j) * p^{(d)}(i, j) * p_k^{(m)}(i, j)$  before and after step 3 of algorithm 1. The improvement in fit after step (3) in Fig. 9 (c,g,k,o) is due to the change in parameters  $W_{sx}$ ,  $W_{sy}$ , and  $W_{d1}$ . Similarly, the improvement in fit after step (3) in Fig. 9 (b,f,j,n,d,h,l,p) is due to the change in parameters  $W_{d2}$ ,  $l_k$ , and  $h_k$ .

### B. Radiograph Deblur

The estimated X-ray source and detector PSFs can be used to reduce blur in radiographs using various deblurring algorithms. We acquired radiograph (Fig. 10 (c,d)) of a star shaped pattern at a SOD of 10mm and ODD of 61mm. The blurry radiograph in Fig. 10 (c) is then deblurred using Wiener filtering and RLS algorithm. The regularization of

both Wiener filtering and RLS methods are adjusted until the noise variance in the red square region in Fig. 10 (e) and (g) are the same. The deblurred radiographs shown in Fig. 10 (e-h) are much sharper than the input radiograph in Fig. 10 (c,d). A scanning electron microscopy (SEM) image of the star artifact in Fig. 10 (a,b) show the slits inside each spoke of the star pattern. By comparing Fig. 10 (f) with Fig. 10 (h), we see that the sharpness of RLS image is better than the Wiener image since the slits in the spokes of the star pattern are more clear in the RLS image.

## VII. CONCLUSION

In this paper, we presented a method to extract both X-ray source and detector blur from radiographs of a Tungsten plate rollbar. Importantly, our method is able to disentangle and estimate the parameters of both X-ray source and detector blur from radiographs that is simultaneously blurred by both sources of blur. We show that blur estimation can be performed using horizontal edge and vertical edge radiographs, each of which is measured at two different values of the ratio of object to detector distance (ODD) and source to object distance (SOD). Using the estimated blur model, we demonstrated the ability to deblur radiographs using various deblurring algorithms.

### APPENDIX A

#### COMPUTING THE IDEAL TRANSMISSION FUNCTION

For every radiograph  $I_k(i, j)$ , the ideal transmission function  $\tilde{T}_k(i, j)$  is estimated from  $I_k(i, j)$  using traditional image processing algorithms. The first step to computing  $\tilde{T}_k(i, j)$  is

to determine the location of the plate's boundary. Even with the rolled edge, the plate is designed such that the transition region from Tungsten to air is no more than one pixel thick. But, from Fig. 5 (a), we can see that it is very difficult to determine the exact pixel locations of the plate's boundary due to blur from the X-ray source and detector. Hence, we scale the radiograph  $I_k(i, j)$  such that it is in the range of 0 to 1 and assume that the edge lies along a iso-valued contour with a level value of 0.5. Such a iso-valued contour is estimated using the marching squares algorithm [41] implemented in the python package *scikit-image* [38].

The ideal transmission function  $\tilde{T}_k(i, j)$  is assigned a value of 0 for the pixels belonging to the Tungsten plate and 1 for the pixels with no plate (or air pixels) since the plate is designed to completely attenuate all X-rays. For the boundary pixels, their values are linearly interpolated given a value of 0.5 along the iso-valued contour and neighboring pixel values of 1 and 0. The iso-valued contour produced by the marching squares algorithm is in the form of a list of real valued  $(k, l)$  coordinates. However, the pixel coordinates  $(i, j)$  of  $\tilde{T}_k(i, j)$  are integer valued. Hence, the values at edge pixel coordinates  $(\lfloor k \rfloor, \lfloor l \rfloor)$ ,  $(\lfloor k \rfloor, \lceil l \rceil)$ ,  $(\lceil k \rceil, \lfloor l \rfloor)$ , and  $(\lceil k \rceil, \lceil l \rceil)$  are determined by interpolation.

To prevent aliasing during convolution,  $\tilde{T}_k(i, j)$  is padded to two times the size of  $I_k(i, j)$  by a special padding procedure that takes into account the orientation of the Tungsten plate (Fig. 5 (b)). The same amount of padding is applied to the top, bottom, left, and right edge of the images. First, a straight line is fit to the sharp edge of the Tungsten plate (Fig. 5 (a)). We extend the straight lines outside the image to account for the plate extending outside the image's field of view. The straight line will split the padded image into two regions, one with the Tungsten plate and another without the plate. Every padded pixel will have a value of 0 or 1 depending on whether it lies in the region with the plate or without the plate.

## APPENDIX B GRADIENT COMPUTATION

To solve the optimization problem in (17), (18), and (19), we use the L-BFGS-B algorithm [35]. Similar to many optimization algorithms such as gradient descent and conjugate gradient, L-BFGS-B needs a routine to calculate the gradient of the objective function in (17), (18), and (19) with respect to the variables that are being optimized. For example, to solve the optimization problem in (17), L-BFGS-B needs to know the gradient of the objective function  $\sum_{k \in \Omega_s} E_k$  with respect to  $s_{sx}$  and  $s_{sy}$ .

We will derive the gradient with respect to all variables for the objective function in (19) (same as (15)). Gradients for solving (17) and (18) will be a trivial extension of the gradient derived for (19). Let the objective function be denoted by  $f$  i.e.,  $f = \sum_{k=1}^K E_k$ . To solve (19), we need the gradient of  $f$ , which is a vector consisting of the partial derivatives  $\frac{\partial f}{\partial s_{sx}}$ ,  $\frac{\partial f}{\partial s_{sy}}$ ,  $\frac{\partial f}{\partial s_{d1}}$ ,  $\frac{\partial f}{\partial s_{d2}}$ ,  $\frac{\partial f}{\partial q}$ ,  $\frac{\partial f}{\partial l_k}$ , and  $\frac{\partial f}{\partial h_k} \forall k$ .

To compute the partial derivatives, we use the chain rule and quotient rule of calculus. First, we will partially compute only that part of the derivative which is common to all parameters

irrespective of whether it belongs to the source PSF, the detector PSF, or the transmission function. Let  $v$  represent any one parameter among  $s_{sx}$ ,  $s_{sy}$ ,  $s_{d1}$ ,  $s_{d2}$ ,  $q$ ,  $l_k$ , and  $h_k$ . Then, the derivative of  $f$  with respect to  $v$  is,

$$\frac{\partial f}{\partial v} = \sum_k \sum_{i,j} w_k(i, j) (I_k(i, j) - \bar{I}_k(i, j)) \frac{\partial \bar{I}_k(i, j)}{\partial v} \quad (22)$$

where  $\bar{I}_k(i, j) = T_k(i, j) * p_k^{(s)}(i, j) * p^{(d)}(i, j) * p_k^{(m)}(i, j)$ . In (22), every term and operator except  $\frac{\partial \bar{I}_k(i, j)}{\partial v}$  is independent of whether  $v$  is  $s_{sx}$ ,  $s_{sy}$ ,  $s_{d1}$ ,  $s_{d2}$ ,  $q$ ,  $l_k$ , or  $h_k$ . Next, we shall expand the derivative  $\frac{\partial \bar{I}_k(i, j)}{\partial v}$ . This requires us to consider source, detector, and transmission function parameters separately.

### A. Variable $v$ is a source PSF parameter

Let  $v$  be one among the source PSF parameters  $s_{sx}$  or  $s_{sy}$ . For compactness of representation, we shall assume  $g_{s,k}(i, j) = \exp\left(-\frac{SOD_k}{ODD_k} \Delta \sqrt{s_{sx}^2 i^2 + s_{sy}^2 j^2}\right)$  and  $Z_{s,k} = \sum_{i,j} g_{s,k}(i, j)$  from (11). Then, using the quotient rule,

$$\frac{\partial \bar{I}_k(i, j)}{\partial v} = T_k(i, j) * \frac{1}{Z_{s,k}^2} \left( Z_{s,k} \frac{\partial g_{s,k}(i, j)}{\partial v} - g_{s,k}(i, j) \frac{\partial Z_{s,k}}{\partial v} \right) * p^{(d)}(i, j) * p_k^{(m)}(i, j), \quad (23)$$

where  $*$  denotes discrete 2D convolution,  $\partial Z_{s,k}/\partial v = \sum_{i,j} \partial g_{s,k}(i, j)/\partial v$ , and

$$\frac{\partial g_{s,k}(i, j)}{\partial v} = \begin{cases} -\frac{g_{s,k}(i, j) SOD_k \Delta s_{sx} i^2}{ODD_k \sqrt{s_{sx}^2 i^2 + s_{sy}^2 j^2}}, & \text{if } v \text{ is } s_{sx}, \\ -\frac{g_{s,k}(i, j) SOD_k \Delta s_{sy} j^2}{ODD_k \sqrt{s_{sx}^2 i^2 + s_{sy}^2 j^2}}, & \text{if } v \text{ is } s_{sy}. \end{cases} \quad (24)$$

### B. Variable $v$ is a detector PSF parameter

Let  $v$  be one among the detector PSF parameters  $s_{d1}$ ,  $s_{d2}$ , or  $q$ . For compactness of representation, we shall assume  $g_{d1}(i, j) = \exp\left(-s_{d1} \Delta \sqrt{i^2 + j^2}\right)$ ,  $g_{d2}(i, j) = \exp\left(-s_{d2} \Delta \sqrt{i^2 + j^2}\right)$ ,  $Z_{d1} = \sum_{i,j} g_{d1}(i, j)$ , and  $Z_{d2} = \sum_{i,j} g_{d2}(i, j)$  from (13) and (14). Using the quotient rule, we get,

$$\frac{\partial \bar{I}_k(i, j)}{\partial v} = T_k(i, j) * p_k^{(s)}(i, j) * \frac{\partial p^{(d)}(i, j)}{\partial v} * p_k^{(m)}(i, j), \quad (25)$$

where  $*$  denotes discrete 2D convolution,

$$\frac{\partial p^{(d)}(i, j)}{\partial v} = \begin{cases} \frac{q}{Z_{d1}^2} \left( Z_{d1} \frac{\partial g_{d1}(i, j)}{\partial v} - g_{d1}(i, j) \frac{\partial Z_{d1}}{\partial v} \right), & \text{if } v \text{ is } s_{d1}, \\ \frac{1-q}{Z_{d2}^2} \left( Z_{d2} \frac{\partial g_{d2}(i, j)}{\partial v} - g_{d2}(i, j) \frac{\partial Z_{d2}}{\partial v} \right), & \text{if } v \text{ is } s_{d2}, \\ \frac{1}{Z_{d1}} g_{d1}(i, j) - \frac{1}{Z_{d2}} g_{d2}(i, j), & \text{if } v \text{ is } q, \end{cases}$$

$$\begin{aligned} \partial g_{d1}(i, j)/\partial v &= -g_{d1}(i, j) \Delta \sqrt{i^2 + j^2}, \quad \partial g_{d2}(i, j)/\partial v = \\ &= -g_{d2}(i, j) \Delta \sqrt{i^2 + j^2}, \quad \partial Z_{d1}/\partial v = \sum_{i,j} \partial g_{d1}(i, j)/\partial v, \quad \text{and} \\ \partial Z_{d2}/\partial v &= \sum_{i,j} \partial g_{d2}(i, j)/\partial v. \end{aligned}$$

### C. Variable $v$ is a transmission function parameter

Let  $v$  be one among the transmission function parameters  $l_k$  or  $h_k$ . Then,

$$\frac{\partial \bar{I}_k(i, j)}{\partial v} = \frac{\partial T_k(i, j)}{\partial v} * p_k^{(s)}(i, j) * p^{(d)}(i, j) * p_k^{(m)}(i, j), \quad (26)$$

$$\text{where } \frac{\partial T_k(i, j)}{\partial v} = \begin{cases} 1 - \bar{T}_k(i, j), & \text{if } v \text{ is } l_k, \\ \bar{T}_k(i, j), & \text{if } v \text{ is } h_k. \end{cases} \quad (27)$$

### ACKNOWLEDGMENT

LLNL-JRNL-760284. This work was performed under the auspices of the U.S. Department of Energy by Lawrence Livermore National Laboratory (LLNL) under Contract DE-AC52-07NA27344. LDRD funding 16-ERD-006 and 19-ERD-022. We thank Kyle Champley from LLNL for useful discussions. We also thank Markus Baier and Professor Simone Carmignato from University of Padova for fabricating and providing the star pattern test object utilized in this manuscript.

### REFERENCES

- [1] H. E. Martz, C. M. Logan, D. J. Schneberk, and P. J. Shull, *X-ray Imaging: fundamentals, industrial techniques and applications*. CRC Press, 2016.
- [2] K. A. Mohan, S. V. Venkatakrishnan, J. W. Gibbs, E. B. Gulsoy, X. Xiao, M. D. Graef, P. W. Voorhees, and C. A. Bouman, "TIMBIR: A method for time-space reconstruction from interlaced views," *IEEE Transactions on Computational Imaging*, vol. 1, no. 2, pp. 96–111, June 2015.
- [3] J. W. Gibbs, K. A. Mohan, E. B. Gulsoy, A. J. Shahani, X. Xiao, C. A. Bouman, M. De Graef, and P. W. Voorhees, "The three-dimensional morphology of growing dendrites," *Scientific Reports*, vol. 5, no. 11824, 2015.
- [4] S. G. Azevedo, H. E. Martz, M. B. Aufderheide, W. D. Brown, K. M. Champley, J. S. Kallman, G. P. Roberson, D. Schneberk, I. M. Seetho, and J. A. Smith, "System-independent characterization of materials using dual-energy computed tomography," *IEEE Transactions on Nuclear Science*, vol. 63, no. 1, pp. 341–350, Feb 2016.
- [5] B. V. Ginneken, B. M. T. H. Romeny, and M. A. Viergever, "Computer-aided diagnosis in chest radiography: A survey," *IEEE Transactions on Medical Imaging*, vol. 20, no. 12, pp. 1228–1241, Dec 2001.
- [6] W. Huda and R. B. Abrahams, "Radiographic techniques, contrast, and noise in x-ray imaging," *American Journal of Roentgenology*, vol. 204, no. 2, pp. W126–W131, 2015.
- [7] Z. Ying, R. Naidu, and C. R. Crawford, "Dual energy computed tomography for explosive detection," *Journal of X-Ray Science and Technology*, vol. 14, pp. 235–256, 2006.
- [8] S. Singh and M. Singh, "Explosives detection systems (EDS) for aviation security," *Signal Processing*, vol. 83, no. 1, pp. 31 – 55, 2003.
- [9] R. Anirudh, H. Kim, J. J. Thiagarajan, K. Aditya Mohan, K. Champley, and T. Bremer, "Lose the views: Limited angle CT reconstruction via implicit sinogram completion," in *The IEEE Conference on Computer Vision and Pattern Recognition (CVPR)*, June 2018.
- [10] E. Shefer, A. Altman, R. Behling, R. Goshen, L. Gregorian, Y. Roterman, I. Uman, N. Wainer, Y. Yagil, and O. Zarchin, "State of the art of CT detectors and sources: A literature review," *Current Radiology Reports*, vol. 1, no. 1, pp. 76–91, Mar 2013.
- [11] H. Li, A. Kingston, G. Myers, B. Recur, and A. Sheppard, "3d X-ray source deblurring in high cone-angle micro-CT," *IEEE Transactions on Nuclear Science*, vol. 62, no. 5, pp. 2075–2084, Oct 2015.
- [12] K. A. Mohan, R. M. Panas, and J. A. Cuadra, "A systems approach to prediction and mitigation of radiographic blur," in *Proceedings of 2018 Summer Topical Meeting on Advancing Precision in Additive Manufacturing*, July 2018, pp. 211–216.
- [13] N. M. De Clerck, K. Meurrens, H. Weiler, D. Van Dyck, G. Vanhoutte, P. Terpstra, and A. A. Postnov, "High-resolution X-ray microtomography for the detection of lung tumors in living mice," *Neoplasia*, vol. 6, no. 4, pp. 374–379, 2004.
- [14] S. Tilley, W. Zbijewski, J. H. Siewerdsen, and J. W. Stayman, "Modeling shift-variant x-ray focal spot blur for high-resolution flat-panel cone-beam CT," in *International Conference on Image Formation in X-Ray Computed Tomography*, vol. 2016. NIH Public Access, 2016, pp. 463–466.
- [15] Q. Wang, Y. Zhu, and H. Li, "Imaging model for the scintillator and its application to digital radiography image enhancement," *Optics express*, vol. 23, no. 26, pp. 33 753–33 776, 2015.
- [16] A. E. S. von Wittenau, C. M. Logan, M. B. Aufderheide, and D. M. Slone, "Blurring artifacts in megavoltage radiography with a flat-panel imaging system: Comparison of monte carlo simulations with measurements," *Medical Physics*, vol. 29, no. 11, pp. 2559–2570, 2002.
- [17] J. D. Everson and J. E. Gray, "Focal-spot measurement: comparison of slit, pinhole, and star resolution pattern techniques," *Radiology*, vol. 165, no. 1, pp. 261–264, 1987.
- [18] E. Loewenthal, E. Loewinger, E. Bar-Avraham, and G. Barnea, "Measurement of the source size of a 6- and 18-MV radiotherapy linac," *Medical Physics*, vol. 19, no. 3, pp. 687–690, 1992.
- [19] A. E. Schach von Wittenau, C. M. Logan, and R. D. Rikard, "Using a tungsten rollbar to characterize the source spot of a megavoltage bremsstrahlung linac," *Medical Physics*, vol. 29, no. 8, pp. 1797–1806, 2002.
- [20] P. Russo and G. Mettivier, "Method for measuring the focal spot size of an x-ray tube using a coded aperture mask and a digital detector," *Medical Physics*, vol. 38, no. 4, pp. 2099–2115, 2011.
- [21] K. S. Sharma, S. Seshadri, M. Feser, and G. Wang, "Accurate resolution measurement for x-ray micro-CT systems," *AIP Conference Proceedings*, vol. 1365, no. 1, pp. 337–340, 2011.
- [22] N. Joshi, R. Szeliski, and D. J. Kriegman, "PSF estimation using sharp edge prediction," in *2008 IEEE Conference on Computer Vision and Pattern Recognition*, June 2008, pp. 1–8.
- [23] E. Kee, S. Paris, S. Chen, and J. Wang, "Modeling and removing spatially-varying optical blur," in *2011 IEEE International Conference on Computational Photography (ICCP)*, April 2011, pp. 1–8.
- [24] B. Hunt, "Deconvolution of linear systems by constrained regression and its relationship to the Wiener theory," *IEEE Transactions on Automatic Control*, vol. 17, no. 5, pp. 703–705, October 1972.
- [25] F. Orieux, J.-F. Giovannelli, and T. Rodet, "Bayesian estimation of regularization and point spread function parameters for Wiener-Hunt deconvolution," *J. Opt. Soc. Am. A*, vol. 27, no. 7, pp. 1593–1607, Jul 2010.
- [26] C. R. Vogel and M. E. Oman, "Fast, robust total variation-based reconstruction of noisy, blurred images," *IEEE Transactions on Image Processing*, vol. 7, no. 6, pp. 813–824, June 1998.
- [27] C. A. Bouman, *Model Based Image Processing*, 2013. [Online]. Available: <https://engineering.purdue.edu/~char~bouman/publications/pdf/MBIP-book.pdf>
- [28] R. Puetter, T. Gosnell, and A. Yahil, "Digital image reconstruction: Deblurring and denoising," *Annual Review of Astronomy and Astrophysics*, vol. 43, no. 1, pp. 139–194, 2005.
- [29] M. N. Hussien and M. I. Saripan, "Computed tomography soft tissue restoration using wiener filter," in *2010 IEEE Student Conference on Research and Development (SCoReD)*, Dec 2010, pp. 415–420.
- [30] A. C. Kak and M. Slaney, *Principles of Computerized Tomographic Imaging*. Society for Industrial and Applied Mathematics, 2001.
- [31] B. H. Hasegawa, *Physics of medical x-ray imaging*, 2nd ed. Medical Physics Pub Corp, 1990.
- [32] J. A. Cuadra and R. M. Panas, "Uncertainty quantification of an X-ray system via a 0D model using a systems approach," in *Proceedings of the Annual Meeting of the American Society for Precision Engineering 31st Annual Meeting*, Oct 2016.
- [33] —, "Uncertainty quantification of an X-ray computed tomography system," in *EUSPEN 2017 Special Interest Group Meeting: Additive Manufacturing*, Oct 2017.
- [34] R. M. Panas, J. A. Cuadra, K. A. Mohan, and R. Morales, "A systems approach to estimating uncertainty in X-ray radiographic metrology," *Manuscript is in preparation*, 2019.
- [35] R. Byrd, P. Lu, J. Nocedal, and C. Zhu, "A limited memory algorithm for bound constrained optimization," *SIAM Journal on Scientific Computing*, vol. 16, no. 5, pp. 1190–1208, 1995.
- [36] E. Jones, T. Oliphant, P. Peterson *et al.*, "SciPy: Open source scientific tools for Python," 2001–. [Online]. Available: <http://www.scipy.org/>
- [37] C. Zhu, R. H. Byrd, P. Lu, and J. Nocedal, "Algorithm 778: L-BFGS-B: Fortran subroutines for large-scale bound-constrained optimization," *ACM Trans. Math. Softw.*, vol. 23, no. 4, pp. 550–560, Dec. 1997.

- [38] S. van der Walt, J. L. Schönberger, J. Nunez-Iglesias, F. Boulogne, J. D. Warner, N. Yager, E. Gouillart, T. Yu, and the scikit-image contributors, "scikit-image: image processing in Python," *PeerJ*, vol. 2, p. e453, 6 2014.
- [39] C. Bouman and K. Sauer, "A generalized gaussian image model for edge-preserving map estimation," *IEEE Transactions on image processing*, vol. 2, no. 3, pp. 296–310, 1993.
- [40] K. A. Mohan, "Design of 4D x-ray tomography experiments for reconstruction using regularized iterative algorithms," in *Developments in X-Ray Tomography XI*, vol. 10391, 2017, p. 103910U.
- [41] W. E. Lorensen and H. E. Cline, "Marching cubes: A high resolution 3d surface construction algorithm," *SIGGRAPH Comput. Graph.*, vol. 21, no. 4, pp. 163–169, Aug. 1987.